Briefings in Bioinformatics, 2026, 27, bbag029
https://doi.org/10.1093/bib/bbag029
Published: 2 February 2026
Problem Solving Protocol

OXFORD

PathCLAST: pathway-augmented contrastive learning with attention for interpretable spatial transcriptomics

Minho Noh[1], Sungkyung Lee[1], Sunghyun Kim[2], Sangsoo Lim[1,*]

[1]Department of Computer Science and Artificial Intelligence, Dongguk University, 30, Pildong-ro 1-gil, Jung-gu, Seoul 04620, South Korea
[2]Division of AI Convergence, Dongguk University, 30, Pildong-ro 1-gil, Jung-gu, Seoul 04620, South Korea

*Corresponding author. E-mail: sslim@dgu.ac.kr

Abstract

Deciphering how molecular programs are spatially organized within tissues is pivotal for understanding tumor evolution and microenvironmental interactions. Existing spatial transcriptomics tools either rely on gene-level features, ignoring the rich topology of biological pathways, or deliver black-box clusters with little mechanistic insight; thus, they limit their translational impact. A method that simultaneously leverages pathway structures and spatially matched histopathology could produce domain delineations that are both accurate and biologically interpretable. We introduce PathCLAST (Pathway-augmented Contrastive Learning with Attention for interpretable Spatial Transcriptomics), which is a framework that integrates gene expression, histopathological images, and curated pathway graphs via bimodal contrastive learning. By embedding expression profiles into biologically structured graphs, and aligning them with local image features, PathCLAST achieves state-of-the-art spatial domain identification on multiple public datasets, while offering pathway-level attention scores for mechanistic interpretation. The pathway embedding also serves as an explicit, biology-informed dimensionality reduction scheme. PathCLAST not only uncovers domain-specific pathways and spatially organized signaling activities, but also quantifies intra-domain heterogeneity, spatial autocorrelation, and inter-domain crosstalk, providing fine-grained insights into tumor progression and tissue architecture. PathCLAST is available at https://github.com/sslim-aidrug/PathCLAST.

Keywords spatial transcriptomics, spatial domain identification, contrastive learning, biological pathways, dimension reduction

Introduction

Spatial transcriptomics technologies offer a unique capability to profile gene expression while preserving spatial context, enabling high-resolution investigations of cellular heterogeneity, tissue architecture, and disease progression *in situ* [1–3]. Advances in high-throughput sequencing and Fluorescence *In Situ* Hybridization (FISH)-based technologies have rapidly expanded the availability of large-scale spatial omics datasets [4]. This rapid expansion has created a need for computational frameworks that integrate multi-modal data and extract biologically meaningful patterns from complex tissue environments. Despite recent progress [5], key challenges remain, including the high dimensionality and sparsity of gene expression data, the frequent mixing of cell types within spots, and complex spatial dependencies that hinder accurate domain segmentation [6–8].

To address these issues, deep learning and graph-based approaches—such as STAGATE [9], ConGI [6], and Hist2ST [8]—have demonstrated improved spatial domain resolution. These methods often integrate spatial proximity and gene expression signals using neural architectures. However, they may remain sensitive to noise or incompleteness in transcriptomic measurements, and are often limited in their ability to fully leverage additional data modalities, such as histopathological images [10, 11]. While earlier statistical frameworks, including BayesSpace [7] and Giotto [12], incorporated spatial priors through Bayesian or hidden Markov random field models to improve spot classification, these methods generally assume spatial smoothness and lack mechanisms to capture gene–gene interactions and gradual transitions between cell states [6, 13]. More recent deep learning models, such as SEDR [14], CCST [15], and DeepST [16] introduced variational embeddings and spatial constraints; yet, often rely on local neighborhood assumptions that may be suboptimal in heterogeneous tumor environments. Efforts to enhance model robustness have led to the adoption of graph neural networks, including attention-based variants as used in STAGATE [9], which focus solely on transcriptomic signals. With the increasing availability of large-scale histological datasets [17, 18], it has become an important avenue to incorporate image features into spatial transcriptomics models for improving biological resolution.

Received: August 7, 2025. **Revised:** December 15, 2025. **Accepted:** January 6, 2026

However, histopathological images offer complementary structural and phenotypic context and have shown utility in predicting gene expression with reasonable accuracy [19]. Approaches such as stLearn [20] and SpaGCN [21] incorporate morphological features from histology to refine graph structures, although image information is typically used only during graph construction and not in the model optimization itself. As a result, these methods may propagate artifacts when morphological features are noisy or weakly correlated with gene expression [6, 9]. Recent multi-modal contrastive learning approaches, including ConST [22] and ConGI [6], attempt to align gene and image modalities by learning shared representations; yet, these models typically rely on abstract embeddings and underutilize curated biological knowledge.

In this study, we present PathCLAST (pathway-augmented contrastive learning with attention for interpretable spatial transcriptomics), a biologically informed framework that integrates gene expression, histopathological images, and curated pathway graphs into a unified contrastive learning paradigm. Unlike previous approaches that treat gene expression as abstract feature vectors, PathCLAST encodes gene expression profiles through biologically structured pathway-level graphs [23, 24], enabling interpretable and functionally meaningful dimension reduction. Through the direct incorporation of curated gene-pathway relationships, PathCLAST ensures that representations are both data-driven and biologically constrained, facilitating a more faithful alignment across modalities. An integrated attention mechanism further enhances interpretability by quantifying the relative contribution of each biological pathway to spatial domain assignments. Evaluated across multiple spatial transcriptomics datasets, PathCLAST improves clustering performance while revealing domain-specific pathway signatures, spatially organized signaling patterns, and intra-domain heterogeneity. In addition, spatial autocorrelation and inter-domain crosstalk analyses demonstrate its capacity to resolve localized biological processes and inter-compartment communication. Collectively, PathCLAST provides a robust and interpretable framework for integrative spatial omics modeling, offering new avenues for uncovering spatially resolved biological mechanisms and informing downstream applications in tissue biology and disease research.

Approach

The proposed PathCLAST can be decomposed into four main parts (Fig. 1).

1. Data pre-processing and pathway-based graph construction for spatial transcriptomics data (see Data preprocessing)
2. Data augmentation of both pathway graphs and image patches (see Data augmentation)
3. Encoder blocks for pathway graphs and paired image patches (see Dual encoder blocks for pathway graph-image features)
4. Joint representation learning between modalities (see Bi-modal contrastive learning)

Datasets

To benchmark our approach, we analyzed five publicly available spatial transcriptomics (ST) datasets: HER2-Amplified Invasive Ductal Carcinoma (IDC) [25], HER2-Positive Breast Tumor (Her2ST) [26], Human Breast Cancer Ductal Carcinoma (BCDC) [27], 10x Visium HD Human Colorectal Cancer (HCRC) [28], and Human Dorsolateral Prefrontal Cortex (DLPFC) [29]. The four datasets (IDC, Her2ST, BCDC, and DLPFC) include pathologist-annotated spatial domains, while HCRC provides gene expression profiles and histopathological images without domain annotations. All datasets provide paired gene expression and histopathological images (see Approach S1 and Table S1 for details in the Supplementary data).

Data preprocessing

All three datasets consist of paired gene expression profiles and histopathological images. Pathway graphs were first constructed using the KEGG pathway database [30]. Pathways lacking edges were removed, leaving 314 graphs covering 4402 genes. Pathway graphs were generated with the KEGGgraph [31] library in R, and gene expression values were assigned as node features. For each spot, gene expression profiles were mapped to these pathway graphs, resulting in 314 pathway graphs collectively denoted as:

$$X_g = \left\{X_g^{(1)}, X_g^{(2)}, \ldots, X_g^{(314)}\right\}$$

Histopathological images were extracted as 112×112 pixel patches from regions corresponding to each spot, denoted X_i (Fig. 1a). To ensure independence across validation folds, image augmentations were applied exclusively within each fixed patch, and each spot-level pair was augmented independently without cross-patch sampling.

Data augmentation

To improve model generalizability, both modalities underwent data augmentation. For each pathway graph in X_g, we applied node dropping and edge perturbation, obtaining

$$X_g^u = \left\{X_g^{u(1)}, X_g^{u(2)}, \ldots, X_g^{u(314)}\right\},$$
$$X_g^v = \left\{X_g^{v(1)}, X_g^{v(2)}, \ldots, X_g^{v(314)}\right\}$$

For image patches X_i, we applied RandomGrayscale and RandomHorizontalFlip from the Torchvision package [32], and noise addition to obtain X_i^u and X_i^v (Fig. 1b). Augmented data pairs were treated as positive samples for contrastive learning.

Dual encoder blocks for pathway graph-image features

Gene expression profiles were projected into low-dimensional embeddings using GraphSAGE [33] with an attention layer to learn pathway-level representations. The graph encoder, denoted as $f^{\text{graph}}(\cdot)$, processed each augmented pathway graph in X_g^u and X_g^v, and produced latent features Z_g^u and Z_g^v for each pathway as follows:

$$Z_g^u = f^{\text{graph}}(X_g^u), \quad Z_g^v = f^{\text{graph}}(X_g^v) \tag{1}$$

Subsequently, the vanilla attention mechanism aggregated the node-level embeddings Z_g^u and Z_g^v into pathway-level representations Z'^u_g and Z'^v_g. For each augmented view $m \in \{u, v\}$ and node index $k = 1, \ldots, n$, let $\{Z_g^{m(1)}, \ldots, Z_g^{m(n)}\}$ be the set of n node embeddings in the pathway graph. The attention score for node k was produced by

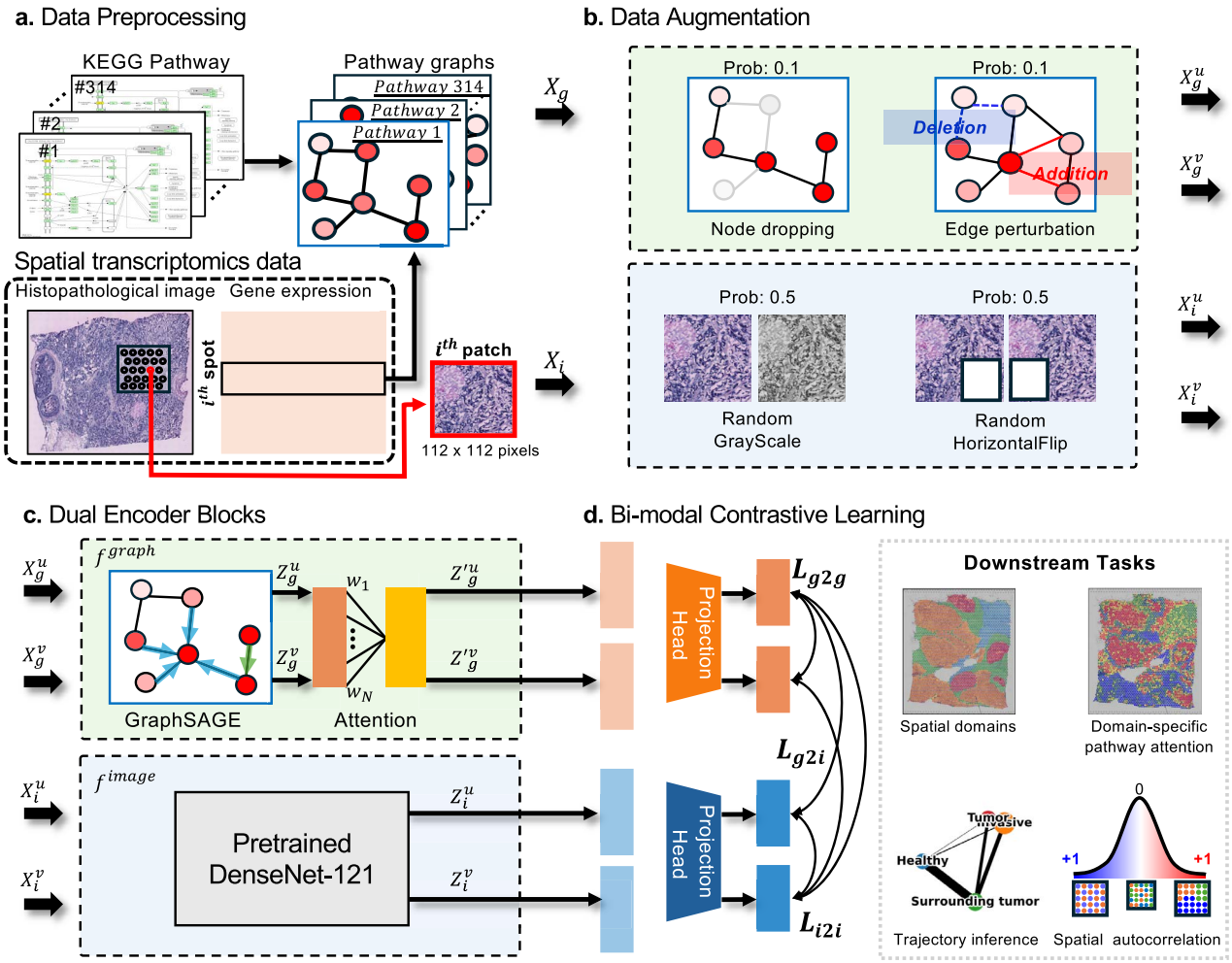

Figure 1 Architecture of the pathway-based spatial transcriptomics data augmentation contrastive learning model. PathCLAST jointly models spatial transcriptomics by integrating gene expression and histopathological image data through pathway-informed contrastive learning. (a) Gene expression profiles are transformed into biologically interpretable pathway graphs, while corresponding histological images are processed into spatially matched patches. (b) Both modalities undergo data-specific augmentations-graph modifications for gene expression graphs and image transformations for image patches-to improve generalization. (c) These augmented data are encoded into low-dimensional embeddings via dedicated encoders. (d) Three contrastive objectives are used to align representations: within gene expression (L_{g2g}), within histological images (L_{i2i}), and across modalities (L_{g2i}). After training, the model embeds raw data into a unified latent space, enabling downstream tasks such as domain-aware clustering, spatial visualization, and trajectory inference.

the shared linear layer:

$$e_m^{(k)} = W \cdot Z_g^{m(k)} + b, \quad m \in \{u, v\} \tag{2}$$

The attention weights were obtained by softmax normalization:

$$\alpha_m^{(k)} = \frac{\exp(e_m^{(k)})}{\sum_{j=1}^{n} \exp(e_m^{(j)})}, \quad \sum_{k=1}^{n} \alpha_m^{(k)} = 1 \tag{3}$$

Finally, the pathway-level embeddings were then given by:

$$Z'^m_g = \sum_{k=1}^{n} \alpha_m^{(k)} Z_g^{m(k)} \tag{4}$$

In parallel, for the image embeddings, DenseNet-121 [34] was adopted as the image encoder. Histopathological images were processed using DenseNet-121 convolutional neural network pre-trained on ImageNet [35]. The image encoder, denoted as $f^{\text{image}}(\cdot)$, processed the augmented image patches X_i^u and X_i^v as follows:

$$Z_i^u = f^{\text{image}}(X_i^u), \quad Z_i^v = f^{\text{image}}(X_i^v) \tag{5}$$

Following the encoding process, to align graph and image representations, a projection head $f^{\text{pro}}(\cdot)$ projected embeddings into a joint latent space. The outputs were:

$$h_g^u = f^{\text{pro}}(Z'^u_g), \quad h_g^v = f^{\text{pro}}(Z'^v_g) \tag{6}$$

$$h_i^u = f^{\text{pro}}(Z_i^u), \quad h_i^v = f^{\text{pro}}(Z_i^v) \tag{7}$$

Bi-modal contrastive learning

We employed contrastive loss function based on the SimCLR framework [36]. Using the projected embeddings obtained from the projection heads, we applied three contrastive loss terms-two within

(graph-to-graph and image-to-image) and one between (graph-to-image). The contrastive learning between modalities aimed to pull paired low-dimensional representations h_g^u and h_i^u of pathway graphs and images together while contrasting those non-matching pairs apart. To better learn the characteristics of each modality, we also performed contrastive learning within each modality for pathway graphs and images, respectively.

We randomly built a minibatch of N spots and defined the contrastive prediction task on paired spots derived from the minibatch, resulting in $2N$ paired spots. We did not explicitly build negative spots. Given a positive pair, we consider the other $2(N-1)$ spots within a minibatch as negative spots. Thus, the within and between contrastive loss functions for positive pairs (h_g^u, h_g^v), (h_i^u, h_i^v) and (h_g^u, h_i^v) can be defined as follows:

1. **Graph-to-graph contrastive loss** (L_{g2g}): Encourages alignment of augmented pathway graph embeddings.
2. **Image-to-image contrastive loss** (L_{i2i}): Aligns augmented image embeddings.
3. **Graph-to-image contrastive loss** (L_{g2i}): Aligns pathway graph embeddings with corresponding image embeddings.

The contrastive loss for a positive pair is defined as:

$$L^1_{h_g^u,h_g^v} = -\log\left(\frac{\exp\left(\frac{sim(h_g^u,h_g^v)}{\tau}\right)}{\sum_{k=1}^{2N} 1_{[k\neq u]}\ \exp\left(\frac{sim(h_g^u,h_g^k)}{\tau}\right)}\right) \tag{8}$$

$$L^2_{h_i^u,h_i^v} = -\log\left(\frac{\exp\left(\frac{sim(h_i^u,h_i^v)}{\tau}\right)}{\sum_{k=1}^{2N} 1_{[k\neq u]}\ \exp\left(\frac{sim(h_i^u,h_i^k)}{\tau}\right)}\right) \tag{9}$$

$$L^3_{h_i^u,h_g^v} = -\log\left(\frac{\exp\left(\frac{sim(h_i^u,h_g^v)}{\tau}\right)}{\sum_{k=1}^{2N} 1_{[k\neq u]}\ \exp\left(\frac{sim(h_i^u,h_g^k)}{\tau}\right)}\right) \tag{10}$$

The indicator term $\mathbf{1}_{[k\neq u]}$ was set to $\mathbf{1}$ when k differs from u, and τ is the temperature hyper-parameter. The similarity measure is defined as:

$$sim(h_i^u,\ h_g^v) = \frac{(h_i^u)^\top h_g^v}{\|h_i^u\|\ \|h_g^v\|} \tag{11}$$

which corresponds to the cosine similarity between the two modality embeddings. The following equations calculate the average contrastive losses L_{g2g}, L_{i2i}, and L_{g2i} overall N pairs in the minibatch as follows:

$$L_{g2g} = \frac{1}{2N}\sum_{k=1}^{N}\left[L^1(2k-1,2k) + L^1(2k,2k-1)\right] \tag{12}$$

$$L_{i2i} = \frac{1}{2N}\sum_{k=1}^{N}\left[L^2(2k-1,2k) + L^2(2k,2k-1)\right] \tag{13}$$

$$L_{g2i} = \frac{1}{2N}\sum_{k=1}^{N}\left[L^3(2k-1,2k) + L^3(2k,2k-1)\right] \tag{14}$$

Finally, the total loss was computed as follows:

$$\mathbf{L} = L_{g2i} + \lambda_1 L_{g2g} + \lambda_2 L_{i2i} \tag{15}$$

where λ_1 and λ_2 were hyper-parameters used to control the contributions of L_{g2g} and L_{i2i} to the final loss, with $\lambda_1 = 0.3$ and $\lambda_2 = 0.2$. To address potential false negatives from in-batch sampling, we additionally implemented a debiased contrastive-learning variant [37] and evaluated sensitivity to batch size and temperature. Full analyses are provided in Supplementary Figure S22.

Evaluation criteria

We used the adjusted rand index (ARI) [38] and normalized mutual information (NMI) [39] as complementary metrics to measure similarity between predicted clusters and ground-truth labels. We also applied Moran's I statistic [40], a measure of spatial autocorrelation that assesses the degree of spatial variability in pathway-level attention scores. ARI accounts for cluster numbers, whereas NMI captures the information shared between predicted and ground-truth clusters (see Approaches S2–S3 in the Supplementary data).

Results

Pathway-guided embedding boosts spatial domain clustering

To evaluate the accuracy and robustness of PathCLAST for spatial domain identification, we benchmarked it across four publicly available spatial transcriptomics datasets (Her2ST, IDC, DLPFC, and BCDC) using the ARI as the primary metric of concordance with ground-truth annotations. To comprehensively position PathCLAST within the current spatial transcriptomics landscape, we compared it against eleven representative approaches spanning expression-only, spatial-graph, multi-modal, graph-attention, and ensemble-based frameworks (see Approaches S4–S5 in the Supplementary data).

Across all datasets, PathCLAST demonstrated consistently high performance (Fig. 2; Supplementary Table S2). In the aggregated ARI comparison (Fig. 2a), PathCLAST achieved the highest median accuracy with a statistically significant margin over the next-best method, ConGI (paired t-test, P =.0347). A robustness analysis comparing minimum versus mean ARI (Fig. 2b) further positioned PathCLAST as the most stable method, exhibiting both strong overall accuracy and favorable worst-case behavior.

Qualitative inspection also supported these findings. On the IDC dataset, PathCLAST produced spatial domain maps that most clearly recapitulated the histological organization of Invasive, DCIS/LCIS, Surrounding-tumor, and Healthy regions (Fig. 2c). UMAP and PAGA representations derived from the learned embeddings (Fig. 2d) showed well-separated clusters and biologically coherent inter-domain relationships. Full spatial predictions, UMAPs, and PAGA graphs [41] for all eleven baselines and PathCLAST are provided for Her2ST (Supplementary Figs S5–S6), DLPFC (Supplementary Figs S7–S8), and BCDC (Supplementary Fig. S9).

To evaluate scalability to higher-resolution platforms, we further applied PathCLAST to two subsets of a VisiumHD human colorectal cancer dataset (6325 and 4685 spots). PathCLAST accurately recovered epithelial, stromal, and immune compartments with clear spatial structure, and its predicted domains showed strong correspondence with cell-type proportions derived from deconvolution analysis

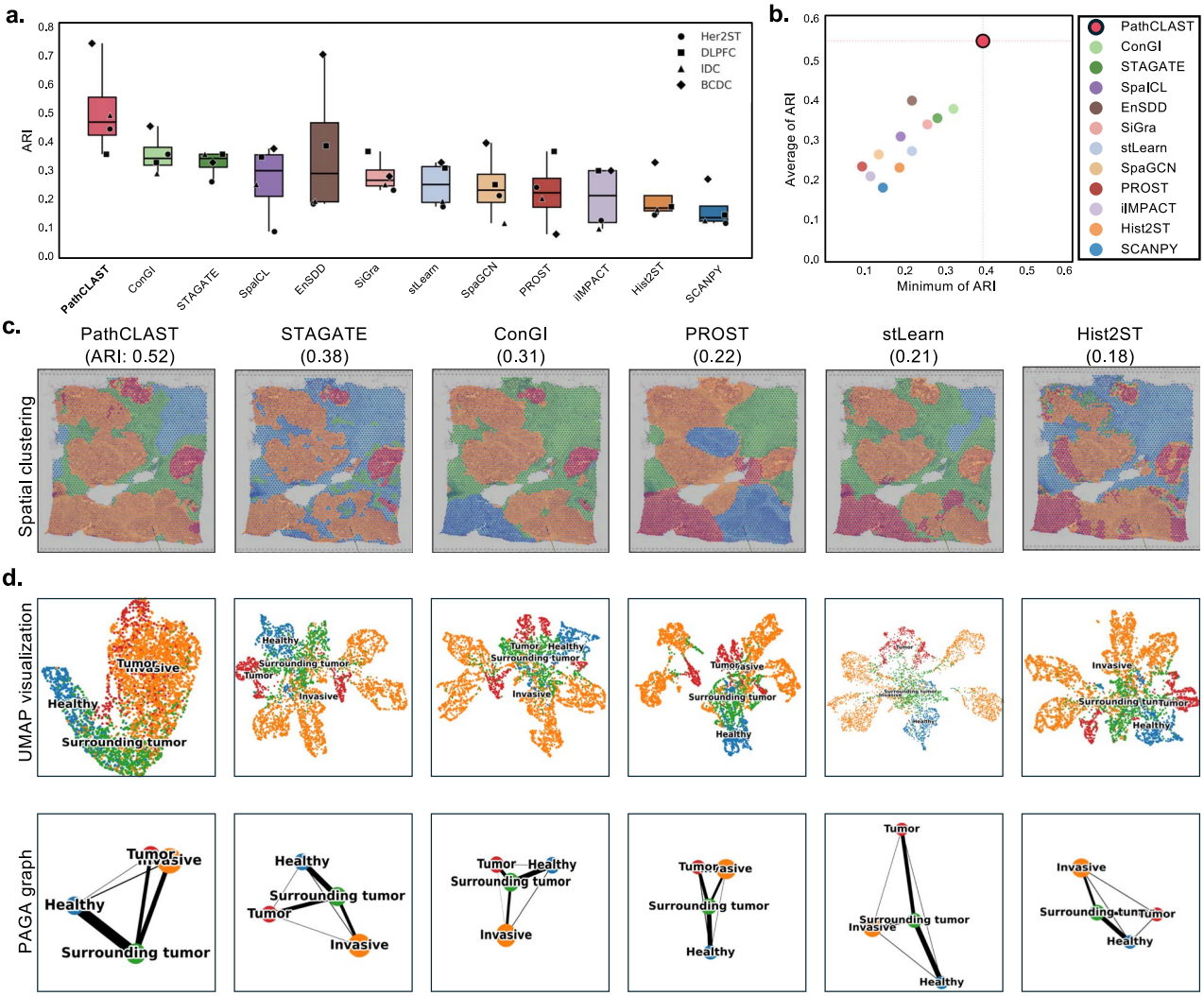

Figure 2 Benchmarking PathCLAST against existing spatial domain identification methods. (a) Comparison of clustering performance (ARI) across four benchmark datasets (Her2ST, DLPFC, IDC, and BCDC). Each boxplot summarizes the distribution of ARI scores across tissue sections within a dataset; individual points denote median ARI for each section (Her2ST, DLPFC) or the dataset-level ARI for single-section datasets (IDC, BCDC). (b) Robustness analysis of baseline methods. For each method, the minimum ARI across datasets is plotted against the mean ARI, illustrating the trade-off between average and worst-case performance. PathCLAST shows both the highest average accuracy and the strongest worst-case robustness. (c) Spatial domain visualizations on the IDC dataset for six representative methods. PathCLAST more clearly delineates major tissue compartments (Invasive, DCIS/LCIS, Surrounding tumor, Healthy) compared with other approaches. Extended results are available in Supplementary Figure S3. (d) UMAP embeddings (top) and PAGA graphs (bottom) derived from the learned representations of each method. PathCLAST produces well-separated domain clusters with biologically coherent connectivity patterns, reflecting clearer transitions between tumor and non-tumor regions relative to baseline methods. For a complete comparison across all the methods, see Supplementary Figure S4.

(Supplementary Fig. S10). These results indicate that PathCLAST generalizes effectively beyond standard-resolution Visium datasets.

Collectively, these results demonstrate that PathCLAST provides accurate, stable, and biologically coherent spatial domain identification across diverse datasets, performing competitively or superior to eleven existing methods while maintaining high robustness and scalability.

Pathway attention reveals domain-specific cancer signatures

We analyzed the pathway-level attention scores derived from our framework to investigate the biological significance of the spatial domains. Each spot-level gene expression was mapped to pathway-specific graphs, enabling PathCLAST to learn which pathways drive the clustering in different tissue regions. A one-way ANOVA followed by Tukey's HSD test (FDR < 0.05) was performed on spot-level spatial attention scores, which identified substantial differences in pathway attention among the four domains: invasive, DCIS/LCIS, surrounding tumor, and healthy regions. Figure 3a presents Venn diagrams illustrating pathways significantly enriched in at least one domain. The full list of pathways, including statistical significance values and domain-specific classifications, is provided in Supplementary Table S3.

To interpret the spatial attention profiles learned by PathCLAST, we examined the pathways assigned the highest and lowest attention weights across spatial domains (Fig. 3b). In invasive regions, PathCLAST prioritized the ErbB signaling pathway, consistent with

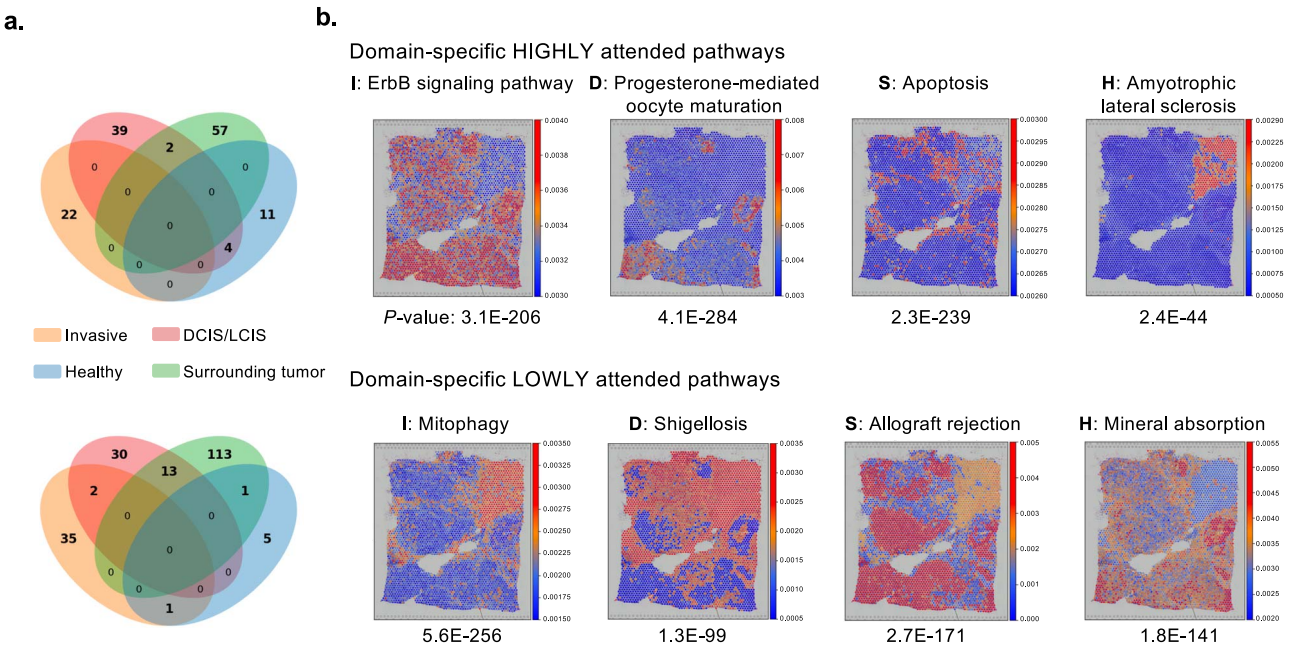

Figure 3 PathCLAST classifies domain-specific highly attended and lowly attended pathways using statistical analysis. (a) Pathway-level ANOVA across tissue labels (invasive, DCIS/LCIS, surrounding tumor, healthy). Pathways that show significant differences then undergo post hoc Tukey's HSD analysis and are compared to the overall mean, allowing their classification as either domain-specific highly attended or lowly attended in each label. The results are visualized via two four-way Venn diagrams-one for domain-specific highly attended pathways (top) and one for domain-specific lowly attended pathways (bottom). (b) Pathways with the strongest domain-specific enrichment in ANOVA results (I: invasive, D: DCIS/LCIS, S: surrounding tumor, H: healthy). See Supplementary Table S3 for full results.

its established role in driving epithelial malignancy [42, 43], while assigning low attention to mitophagy-related pathways, suggesting that mitochondrial quality control processes were less influential for classifying the invasive signature [44]. In DCIS/LCIS domains, high attention to the progesterone-mediated oocyte maturation pathway aligned with hormone-responsive proliferative features [45], whereas Shigellosis-related pathways were less emphasized, consistent with the limited relevance of pathogen response signatures in pre-invasive lesions [46]. Within the Surrounding tumor microenvironment, apoptosis pathways received high attention, potentially reflecting tissue remodeling and immune-mediated clearance [47], while allograft rejection pathways were less informative [48]. In healthy tissue, PathCLAST assigned high attention to the amyotrophic lateral sclerosis (ALS) pathway, potentially indicating the presence of homeostatic stress responses [49, 50], and low attention to mineral absorption pathways, suggesting that nutrient transport features were not discriminative.

Collectively, there were 310 pathways found to be significantly associated with domain classification (**FDR** < 0.05). Notably, Terpenoid backbone biosynthesis exhibited the strongest domain-specific enrichment (FDR = 1.4×10^{-303}), highlighting the metabolic reprogramming characteristic of malignant tissues. The majority of highly attended pathways displayed domain-specific patterns, while lowly attended pathways helped suppress background biological signals, improving domain separability. For example, the high attention assigned to ErbB signaling across both Tumor and Surrounding regions hints at paracrine signaling interactions shaping the tumor microenvironment [51–53]. Similarly, domain-specific high attention to ALS pathways in Healthy regions may reflect protective cellular mechanisms maintaining tissue integrity. Overall, domain-specific pathway signatures derived from PathCLAST attention scores offer biological interpretability beyond data-driven clustering by identifying molecular processes underlying spatial organization and disease progression.

A complementary analysis correlating image-derived principal components with pathway attention weights without using spatial domain information further demonstrated that histopathological features align with distinct molecular programs; details are provided in Supplementary discussion and Supplementary Figure S11.

Intra-domain heterogeneity reveals spatially diverse tumor programs

While domain-specific analysis reveals pathways distinguishing different spatial regions, tumors are intrinsically heterogeneous even within the same pathological domain. To capture such diversity, spatial intra-domain heterogeneity (sIDH) was quantified by calculating the coefficient of variation (CV) of spot-level pathway attention scores within each labeled spatial domain (e.g. invasive, DCIS/LCIS, surrounding tumor, and healthy domain). Figure 4a categorizes sIDH across six biological pathway groups. Among these, metabolic pathways (MT) exhibited a distinctive pattern: invasive regions demonstrated uniformly high IDH, whereas DCIS/LCIS, surrounding tumor, and healthy regions displayed a lower and more consistent level of heterogeneity across pathways within the same category. This consistent metabolic heterogeneity in invasive regions suggests pervasive spatial metabolic reprogramming, consistent with the known metabolic plasticity and adaptation observed in aggressive tumors [54, 55]. In contrast, pathways related to organismal systems (OS), environmental information processing (EIP), genetic information processing (GIP), and human diseases (HD) exhibited a broader distribution of heterogeneity within Invasive regions, indicating that proliferative, signaling, immune,

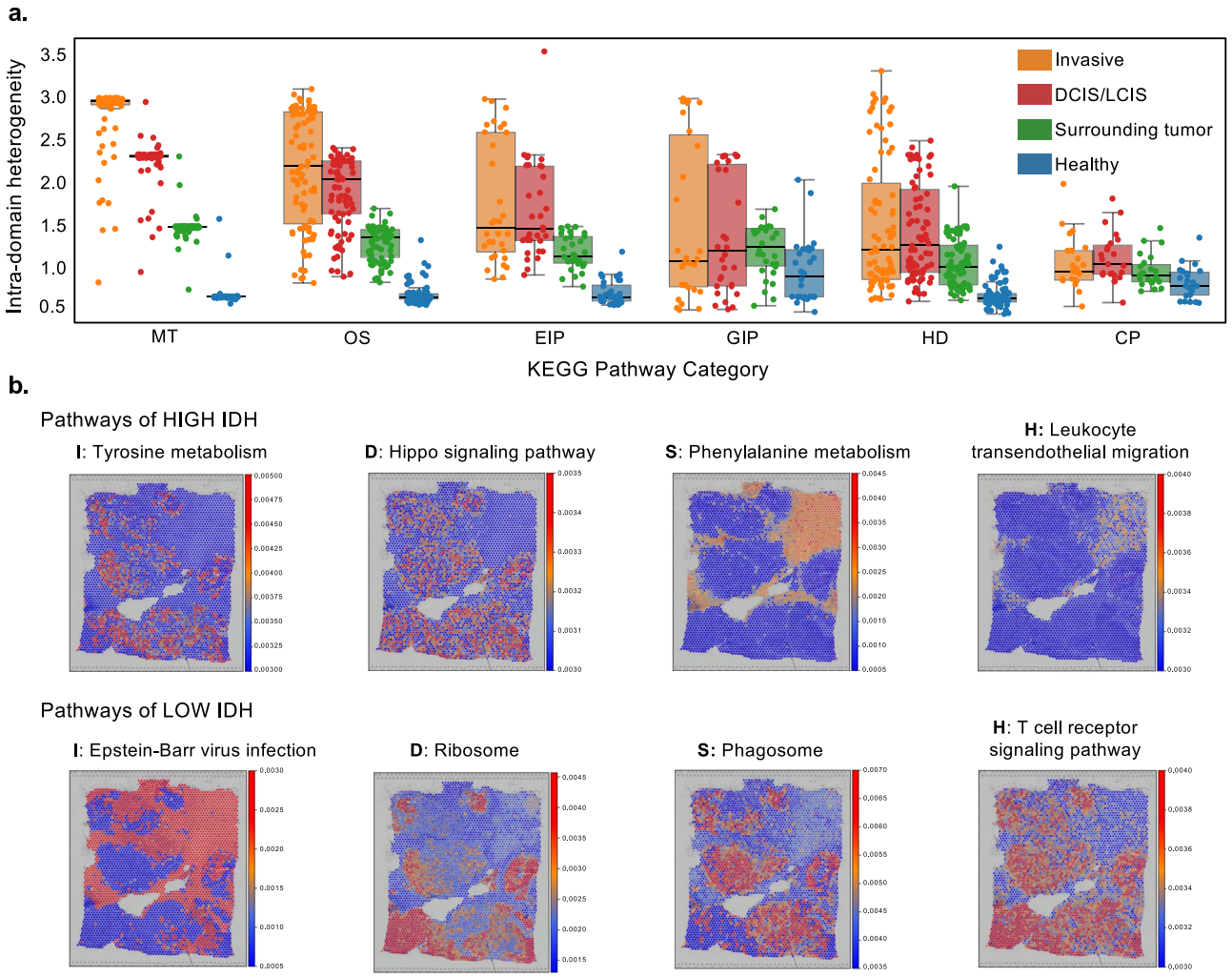

Figure 4 PathCLAST analyzes intra-domain heterogeneity of pathway categories across four tumor-related labels. (a) Boxplot of the computed intra-domain heterogeneity expressed as coefficient of variation for each pathway category-namely, MT (metabolism), OS (organismal Systems), EIP (environmental information processing), GIP (genetic information processing), HD (human diseases), and CP (cellular processes). (b) Spatial visualization of pathways with high intra-domain heterogeneity (top) and pathways with low intra-domain heterogeneity (bottom).

and disease-related programs are spatially variable across tumor subregions [56, 57]. This variability was less pronounced in non-invasive compartments, where pathway attention scores were more tightly distributed.

To further illustrate sIDH patterns, Fig. 4b presents spatial maps of selected pathways with either high or low sIDH. Among pathways with high IDH, tyrosine metabolism (CV = 3.30) attention scores varied substantially within invasive regions, while the Hippo signaling pathway (CV = 3.97) exhibited pronounced variability across DCIS/LCIS domains. Spatial heterogeneity of Phenylalanine metabolism (CV = 1.51) in surrounding tumor regions suggests localized immune or viral mimicry dynamics, whereas leukocyte transendothelial migration (CV = 0.78) showed unexpectedly high variability even within healthy tissue compartments. In contrast, pathways with low sIDH included Epstein-Barr virus infection (CV = 0.49) in invasive, ribosome (CV = 0.33) pathways in DCIS/LCIS, phagosome (CV = 0.63) in surrounding tumor, and T cell receptor signaling pathway (CV = 0.42) in healthy regions. Together, these observations suggest that, although specific signaling and immune-modulatory pathways exhibit high spatial heterogeneity, core housekeeping, and immune-maintenance pathways tended to show lower variability within each domain. In addition, high sIDH was observed in the chemical carcinogenesis (CV = 3.30) and primary immunodeficiency (CV = 2.07), particularly within invasive and surrounding tumor regions. Healthy tissue also exhibited localized variability, with pathways such as RNA degradation (CV = 2.16) showing elevated CV values, indicating heterogeneity in RNA-processing machinery that aligns with the reported differential expression of genes involved in RNA degradation between breast tumors and adjacent normal tissue [58]. The full pathway list of CV values is provided in Supplementary Table S4.

Spatial IDH of pathway attention scores suggests that histologically homogeneous tumor regions harbor molecularly distinct subpopulations with divergent proliferative, metabolic, and stress-response profiles. Such fine-grained diversity may underlie variable therapeutic responses, metastatic potential, and immune evasion within tumors [59, 60]. The ability to map these subdomain-specific pathway attention scores could facilitate more precise therapeutic targeting, especially in heterogeneous tumors where localized aggressive subclones may drive clinical progression. The ability of PathCLAST to spotlight these varying pathway attentions at sub-domain resolution suggests

its potential for informing personalized therapeutic strategies, e.g., by targeting subregions with elevated ErbB signaling pathway activity that may drive invasiveness or metastasis [42, 53].

To assess whether intra-domain pathway heterogeneity reflects underlying cellular diversity, we compared sIDH with cell-type diversity estimated by cell2location [61] using the Human Cell Atlas [62] as reference (Supplementary Fig. S12). Cell-type diversity was quantified as Shannon entropy of spot-level cell-type proportions. Although cell-type diversity exhibited a similar range across all four domains, PathCLAST uncovered pronounced differences in pathway-level heterogeneity. Healthy regions showed uniformly low sIDH, surrounding tumor and DCIS/LCIS displayed moderate levels, and invasive regions exhibited markedly elevated pathway heterogeneity in regions of diversified cell types. This divergence indicates that PathCLAST captures biologically meaningful molecular variation that is not explained by cell-type mixtures alone. In other words, even when cellular diversity is comparable, malignant domains show substantially greater pathway-level dispersion-reflecting microenvironmental complexity, signaling dysregulation, and metabolic heterogeneity characteristic of tumor progression.

Spatial autocorrelation uncovers pathway organization within tumors

We performed a spatial autocorrelation analysis to characterize how pathway activities are organized within and across domains (Fig. 5). Using domain-specific spatial graphs, we applied the Markov Cluster Algorithm (MCL) [63] to subdivide each predicted domain into finer sub-domains (Fig. 5a). This procedure revealed four Invasive clusters (I1–I4), two DCIS/LCIS clusters (D1–D2), three surrounding-tumor clusters (S1–S3), and three healthy clusters (H1–H3), capturing spatially coherent micro-regions within each histological class.

For every sub-domain, we computed Moran's I on pathway attention scores to quantify the degree of spatial autocorrelation (Approach S6 in the Supplementary data). The resulting distributions (Fig. 5b) showed that Invasive clusters generally exhibit higher Moran's I than healthy clusters, indicating stronger spatial structuring of pathway activities in malignant compartments. To assess whether spatial patterns are conserved across tumor micro-regions, we compared Moran's I profiles between pairs of clusters. As an example, Fig. 5c displays the correlation of Moran's I between Invasive clusters I1 and I2, where pathways such as cell cycle and phenylalanine metabolism fall along the high-high diagonal, suggesting conserved spatially restricted proliferation and metabolic programs across distinct invasive niches.

At the functional category level, pathways assigned to organismal systems (OS), environmental information processing (EIP), and metabolism (MT) were predominant among pathways with Moran's I values above the cluster median (Fig. 5d). This indicates that spatial organization within tumors is particularly enriched for proliferative signaling, immune communication, and metabolic reprogramming pathways.

To illustrate these findings, we visualized the spatial distributions of selected high- and low-autocorrelation pathways (Fig. 5e). Among pathways exhibiting strong clustering, the Prolactin signaling pathway (Moran's I = 0.64) and the Rap1 signaling pathway (Moran's I = 0.46) displayed regionally localized attention scores within Invasive and DCIS/LCIS domains, respectively. These localized patterns suggest that spatially constrained localization of growth and adhesion pathways may underpin intratumoral niche formation and local progression. In contrast, pathways such as the T cell receptor signaling pathway (Moran's I = –0.09) and Vitamin B6 metabolism (Moran's I = –0.04) were more spatially dispersed, indicating broader tissue-level engagement of immune and metabolic programs. The spatially localized attention of the Prolactin signaling pathway in invasive domains may reflect its known role in promoting tumor cell proliferation, angiogenesis, and survival in the breast tumor microenvironment [64–66]. Likewise, the regional clustering of Rap1 signaling pathway in DCIS/LCIS regions is consistent with its established function in regulating cell adhesion, polarity, and junctional integrity, processes that are critical during early tumor progression and local invasion [67, 68]. These spatially organized signaling programs highlight how tumors compartmentalize key molecular activities to support progression and adaptation to local microenvironmental cues. DCIS/LCIS regions exhibited strong clustering, with the Rap1 signaling pathway (D2-EI) showing pronounced clustering, reflecting localized activity associated with DCIS/LCIS microenvironments. In Invasive regions, the prolactin signaling pathway (I1-OS) and glycerophospholipid metabolism (I1-MT) demonstrated high Moran's I values, indicative of spatially localized activation, whereas pathways such as the JAK-STAT signaling pathway (I1-EI) displayed broader distributions, suggesting spatial dispersion. In Healthy regions, ABC transporters (H1-EI) exhibited strong clustering, while pathways like Vitamin B6 metabolism (H1-MT) showed a random spatial organization.

Complementary analyses in the Supplementary Materials further support these patterns. Pairwise correlations of pathway-level Moran's I between domains (Supplementary Fig. S14) reveal distinct inter-domain correlation structures, with tumor domains (Invasive and DCIS/LCIS) sharing more similar spatial autocorrelation profiles than Healthy regions. Ranking pathways by Moran's I (Supplementary Figs S15–S16) highlights that highly structured pathways are enriched for signaling, adhesion, immune, and metabolic programs. Scatterplots of Moran's I versus CV within each sub-domain (Supplementary Fig. S17) show that, in tumor regions, pathways with strong spatial clustering also tend to exhibit high intra-domain heterogeneity. Finally, detailed views of invasive sub-domain I1 and DCIS/LCIS sub-domain D2 (Supplementary Fig. S18) illustrate how specific pathways-such as phenylalanine metabolism, ferroptosis, focal adhesion, and Rap1 signaling-combine high Moran's I with elevated CV and form distinct spatial hotspots.

Together, these results demonstrate that PathCLAST not only identifies domain-specific pathway enrichments but also resolves the spatial architecture of pathway activities within tumors. By distinguishing spatially clustered from spatially diffuse pathways and linking them to biologically interpretable programs, PathCLAST provides a detailed view of how malignant tissues compartmentalize signaling, metabolic, and immune processes across the tumor microenvironment.

Inter-domain pathway crosstalk highlights spatially coordinated tumor programs

To investigate how spatially distinct regions coordinate biological processes during tumor progression, we performed a domain-level crosstalk analysis by constructing spatially resolved pathway interaction Map (SPIM) by computing Cross-Moran's I (CMI) of pathway attention scores across domain clusters (Fig. 6a, See Approach S7 in the Supplementary data). CMI quantifies the spatial similarity of pathway attention scores between two adjacent regions, revealing how

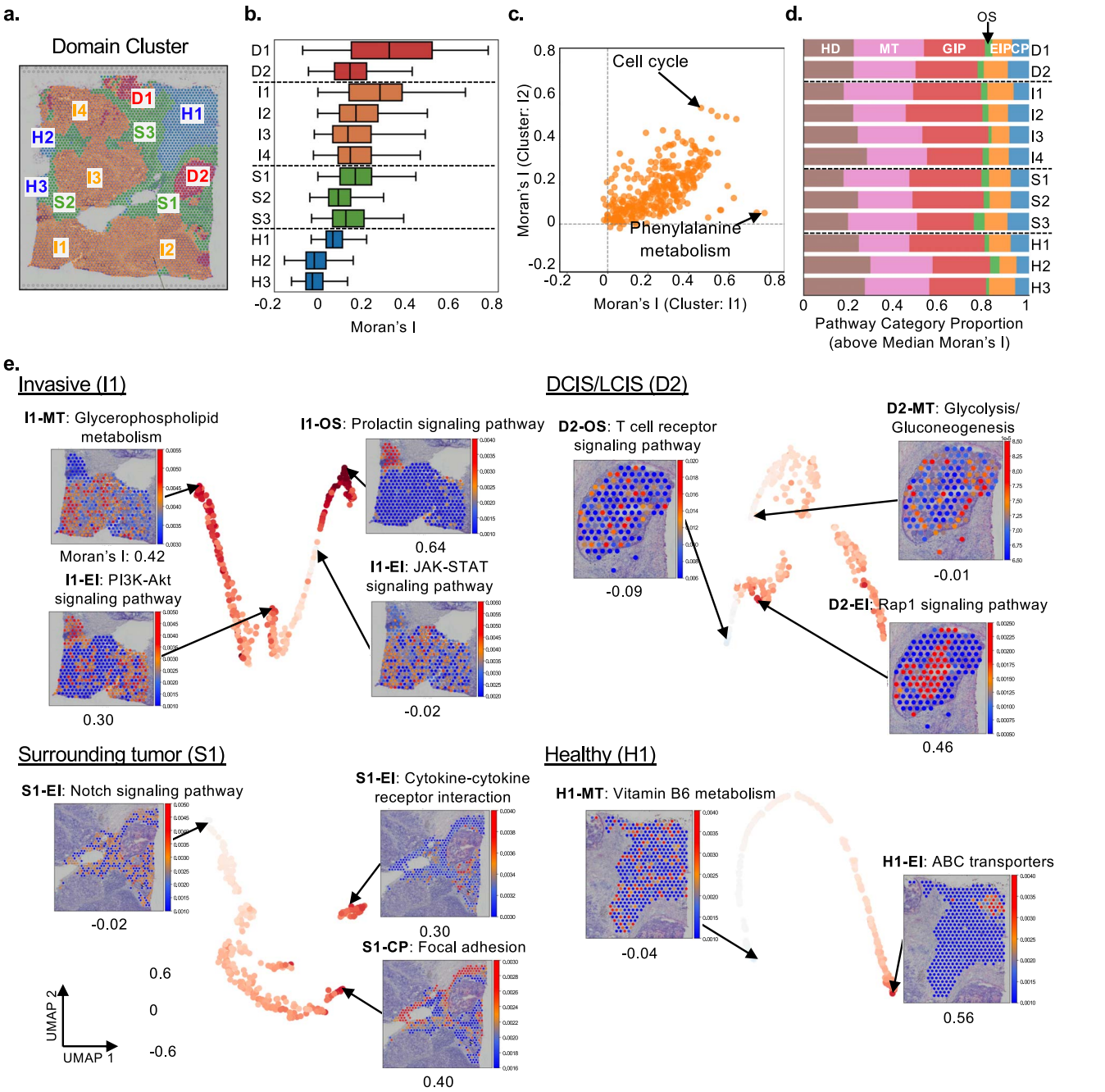

Figure 5 PathCLAST analyzes the spatial autocorrelation of pathway attention among sub-domains. (a) For each domain, MCL clustering is performed to further subdivide the domain. (b) After MCL clustering, pathway attention weights within each cluster are used to calculate Moran's I, and the resulting distributions are visualized using boxplots. (c) The correlation of Moran's I between two clusters (I1, I2) is presented as a scatterplot, with pathways corresponding to high data point values indicated. (d) A bar plot displays the proportion of pathway categories for pathways with Moran's I values above the cluster median. (e) The computed Moran's I values are visualized using UMAP, with each data point representing the Moran's I value for a pathway. In addition, a spatial visualization of pathway attention weights-filtered by cluster-is provided. A detailed schematic of the entire workflow is available in the Supplementary Figure S13.

molecular programs interact across tumor boundaries. The resulting network showed strong cross-domain interactions between Invasive, DCIS/LCIS, and Surrounding tumor regions, with fewer high-strength connections involving healthy tissue. Particularly, Invasive regions exhibited extensive crosstalk with both adjacent tumor edge (surrounding tumor) and DCIS/LCIS compartments, highlighting the interconnected nature of malignant progression.

We examined pathways with high CMI scores to support the functional relevance of these spatial crosstalk patterns (Fig. 6b). Notably, the Hippo signaling pathway (highly attended in DCIS/LCIS, D1) and the cytokine–cytokine receptor interaction pathway (invasive region, I4) exhibited strong crosstalk at $SPIM_1$. This is biologically plausible given that the Hippo pathway integrates mechanical and inflammatory cues to regulate tumor growth and metastasis [69, 70],

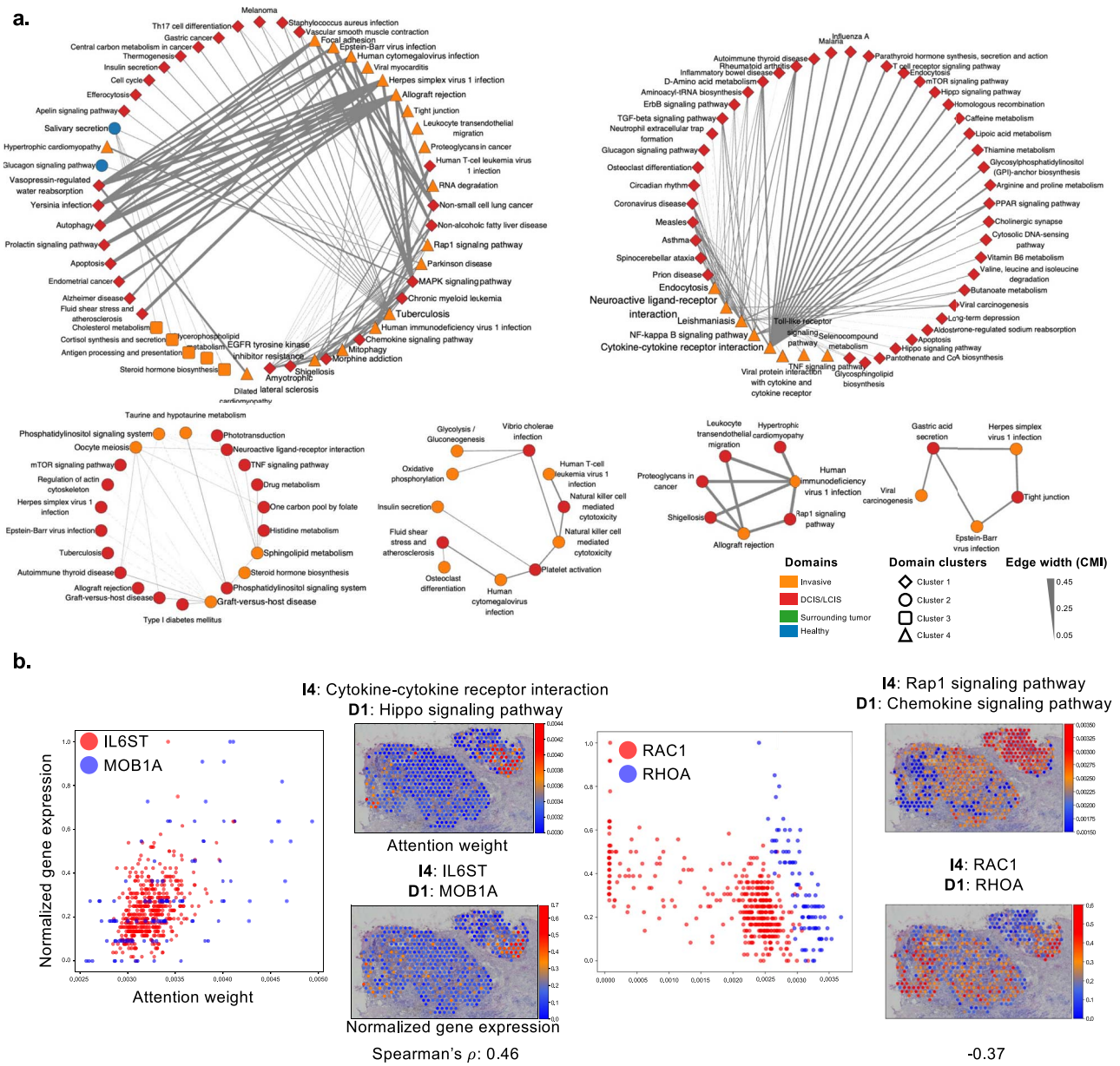

Figure 6 PathCLAST captures spatially resolved pathway crosstalk between domains. (a) A set of SPIMS ($SPIM_1$ to $SPIM_6$ in descending order of size) constructed by computing CMI for pairs of domain clusters. Edge width indicates CMI values. (b) Pathway attention weights for pathways exhibiting crosstalk and the corresponding normalized gene expression data for genes within each pathway are presented through spatial visualization. Additionally, scatter plots depict the correlation between pathway attention weights and normalized gene expression levels.

and cytokine–cytokine receptor interaction pathway modulates Hippo signaling pathway activity through NF-κB-mediated inflammatory responses [71]. Similarly, crosstalk between the Rap1 signaling pathway (I4) and the chemokine signaling pathway (D1) was observed at $SPIM_2$, reflecting dynamic regulation of tumor cell migration and invasion strategies. Rap1 and Rho GTPase circuits orchestrate transitions between mesenchymal and amoeboid motility modes, which are crucial for overcoming extracellular matrix barriers during metastasis [72, 73]. Spatial scatterplots further supported these findings: within overlapping tumor regions, RAC1 (Rap1 signaling pathway) and RHOA (Cytokine-cytokine receptor interaction pathway) gene expression levels displayed a mutually inhibitory correlation pattern (Spearman's ρ = –0.37), consistent with previously described models of plasticity in tumor invasion modes [74, 75].

Together, these analyses demonstrate that spatial pathway crosstalk, as revealed by CMI, captures the dynamic interplay of proliferative, inflammatory, and migratory programs across tumor progression stages. By resolving not only domain-specific pathway attention scores but also their spatial inter-connectivity, PathCLAST provides a more comprehensive view of tissue remodeling in cancer evolution.

Discussion

This study introduces PathCLAST, a pathway-augmented contrastive learning framework that integrates molecular, spatial, and histopathological information to achieve biologically structured and interpretable spatial domain identification. By embedding

gene expression into curated KEGG pathway graphs and learning pathway-level attention scores, the model provides a representation that is both robust to data sparsity and directly tied to mechanistic biological processes. Across four benchmark datasets, PathCLAST consistently outperformed or matched eleven competing methods, demonstrating strong accuracy, stability, and biological coherence.

A central contribution of PathCLAST is its pathway-centric design. Whereas prior multi-modal spatial transcriptomics frameworks such as SpaICL [76] and ConGI [6] apply contrastive learning to unstructured gene-level features, PathCLAST organizes expression data through curated pathway graphs and quantifies their local relevance through pathway attention. This design enables a mechanistic interpretation rarely accessible in existing domain-identification algorithms. Furthermore, by linking spatial organization with pathway activity, PathCLAST bridges molecular processes with histological context and facilitates downstream biological analysis-including intra-domain heterogeneity, spatial autocorrelation, and inter-domain pathway crosstalk.

Beyond domain identification, PathCLAST captures multi-scale spatial organization in tumor microenvironments. Pathway attention revealed domain-specific signatures associated with proliferation, immune activity, metabolic rewiring, and cell-matrix remodeling. Intra-domain heterogeneity analysis further showed that pathway variability captures subtle spatial programs that gene-level features fail to resolve. Notably, the Invasive domain displayed the strongest pathway variability and spatial autocorrelation, consistent with localized regions of metabolic acceleration, mechanical remodeling, and migratory activity. Spatial crosstalk analysis uncovered coordinated signaling between adjacent compartments, including interactions between Hippo signaling and cytokine—mediated inflammatory pathways, or between Rap1 signaling and chemokine pathways—highlighting the functional interdependence between early lesions, invasive fronts, and surrounding tumor niches.

Trajectory inference further demonstrated how spatially distinct tumor compartments may be embedded within a continuous progression axis (Supplementary Fig. S21). In the IDC dataset, spatial trajectory reconstruction using pathway clusters revealed a coherent direction from Invasive regions toward tumor-adjacent tissue and ultimately toward normal epithelium, suggesting that pathway-level embedding organizes tissue structure along biologically meaningful gradients. This offers an orthogonal perspective to static domain assignments and provides a framework for studying spatial evolution in tumorigenesis.

While PathCLAST is primarily designed for spatial-domain detection, complementary frameworks address related analytical tasks. SiGra [77] leverages graph attention to enhance spatial smoothness, whereas SpaIM [78] focuses on imputing unmeasured genes through style-transfer from scRNA-seq profiles. Although SpaIM does not directly target spatial clustering, its imputation capabilities may serve as a valuable upstream module, particularly for datasets with extreme dropout such as DLPFC, potentially enhancing pathway-graph construction in future versions of PathCLAST.

We also note that the relative performance of multi-modal models such as ConGI [6] and Hist2ST [8] can vary across datasets. Because these methods incorporate histopathology, their accuracy can be more sensitive to differences in staining quality, imaging resolution, and tissue morphology across studies. In contrast, STAGATE-relying solely on spatial transcriptomic features-tends to exhibit more stable cross-dataset performance. This helps explain why STAGATE performs more robustly in our expanded benchmark despite ConGI reporting higher performance in its original publication.

The pathway-graph embedding used in PathCLAST requires sufficient gene coverage to obtain meaningful representations. Thus, the method is currently less suited for low-gene-count platforms such as Xenium, which typically measure only several hundred transcripts. Nevertheless, the model demonstrated strong scalability on large high-resolution datasets, including VisiumHD sections with over 130 000 spots. Future work will focus on adaptive pathway reconstruction strategies to extend PathCLAST to sparse-gene ST platforms and to better integrate scRNA-seq imputation methods into the pipeline.

From a biological perspective, the spatial heterogeneity uncovered within each domain has potential clinical relevance. Different subregions of invasive tumors exhibited distinct pathway signatures, suggesting localized niches that may harbor therapy-resistant or metastasis-initiating populations. Mapping these intra-domain variations could inform precision therapeutic strategies that target spatially confined signaling axes. Although our current analyses focus on single-patient sections, extending PathCLAST to multi-patient cohorts will be essential for assessing the generalizability of identified pathway signatures and for determining whether pathway attention profiles can serve as transferable biomarkers of tumor architecture.

Finally, integrating pathway attention profiles with clinical outcome data represents a promising direction for next-generation spatially informed cancer stratification. Pathway-level spatial patterns may reveal prognostic domains, microenvironmental vulnerabilities, and actionable signaling dependencies that are not detectable from bulk or single-cell data alone. In this context, the interpretability, robustness, and biological grounding of PathCLAST make it well suited for supporting spatially targeted therapeutic strategies and advancing the development of mechanism-aware spatial transcriptomic models. Please refer to supplementary discussions including figures from S22 to S25 on robustness, feature stability, and ablation analyses of our study.

Conclusion

We present PathCLAST, a pathway-augmented contrastive learning framework that integrates KEGG-based pathway graphs with histopathological image features for spatial transcriptomics analysis. By projecting gene expression onto curated pathway structures, PathCLAST performs biologically grounded dimension reduction that is more stable and noise-robust than HVG-based approaches, while enabling direct pathway-level interpretability. Through bi-modal contrastive learning, PathCLAST produces unified embeddings that outperform existing methods across multiple spatial transcriptomics benchmarks. Beyond accurate spatial domain identification, the framework reveals domain-specific pathway activity, intra-domain molecular heterogeneity, spatially organized signaling patterns via Moran's I, and cross-compartment crosstalk through Cross-Moran's I. These insights illustrate how pathway-informed modeling captures both local and global tissue organization. Overall, PathCLAST provides an interpretable and biologically structured alternative to conventional feature selection, offering a robust foundation for spatial systems biology and future applications in microenvironment profiling and precision oncology.

Key Points

- PathCLAST combines gene expression, histopathology, and curated pathway graphs in a bi-modal contrastive learning framework to enhance spatial domain identification.
- Pathway-guided embeddings provide biologically structured dimension reduction, yielding more accurate and more stable clustering performance than HVG-based and existing multi-modal methods across multiple datasets.
- Domain-specific pathway attention maps reveal the molecular processes defining each tissue compartment, enabling mechanistic and interpretable biological insights.
- Intra-domain heterogeneity and Moran's I-based spatial autocorrelation analyses characterize pathway stability and spatial organization within tumor and non-tumor regions.
- The spatial pathway interaction map quantifies statistically significant crosstalk between domains, highlighting localized inter-domain signaling networks.

Author contributions

Minho Noh was responsible for software, methodology, formal analysis, and writing—original draft. Sungkyung Lee contributed to formal analysis and investigation. Sunghyun Kim was responsible for validation. Sangsoo Lim was responsible for conceptualization, supervision, and writing—review & editing.

Supplementary data

Supplementary data is available at *Briefings in Bioinformatics* online.

Conflict of interest

The authors declare that they have no conflict of interest.

Funding

This work was supported by the Ministry of Science and ICT (MSIT), Korea, under the Information Technology Research Center (ITRC) support program supervised by the Institute for Information and Communications Technology Planning and Evaluation (IITP) [IITP-2025-RS-2020-11201789]; the Artificial Intelligence Convergence Innovation Human Resources Development program supervised by the IITP [IITP-2025-RS-2023-00254592]; and the National Research Foundation of Korea (NRF) grant funded by the Korea government (MSIT) [RS-2025-00560523, RS-2024-00346342]; and Korean ARPA-H Project through the Korea Health Industry Development Institute (KHIDI), funded by the Ministry of Health & Welfare, Republic of Korea (grant number: RS-2024-00512120).

Data availability

Raw datasets were obtained directly from their original sources. (i) Human breast cancer datasets generated with the 10x Visium platform-such as the HER2-amplified invasive ductal carcinoma (IDC) [25] dataset (www.10xgenomics.com/datasets/human-breast-cancer-IDC); (ii) The HER2-positive breast-tumor dataset (Her2ST) [26] is available at (github.com/almaan/her2st); (iii) The Visium FFPE Human Breast Cancer dataset (BCDC) [27] is available at (www.10xgenomics.com/datasets/breast-cancer-FFPE); (iv) The Visium HD Human Colorectal Cancer dataset (HCRC) [28] is available at (www.10xgenomics.com/datasets/visium-hd-human-crc); and (v) The 10x Visium Human dorsolateral prefrontal cortex (DLPFC) [29] data are available at LIBD (research.libd.org/spatialLIBD). For PathCLAST, the source code is available at GitHub: https://github.com/sslim-aidrug/PathCLAST.

References

1. Marx V. Method of the year: spatially resolved transcriptomics. *Nat Methods* 2021;**18**:9–14. https://doi.org/10.1038/s41592-020-01033-y
2. Maynard KR, Collado-Torres L, Weber LM. *et al.* Transcriptome-scale spatial gene expression in the human dorsolateral prefrontal cortex. *Nat Neurosci* 2021;**24**:425–36. https://doi.org/10.1038/s41593-020-00787-0
3. Jun D, An Z-J, Huang Z-F. *et al.* Novel insights from spatial transcriptome analysis in solid tumors. *Int J Biol Sci* 2023;**19**:4778–92. https://doi.org/10.7150/ijbs.83098
4. Cheng A, Guanyu H, Li WV. Benchmarking cell-type clustering methods for spatially resolved transcriptomics data. *Brief Bioinform* 2023;**24**:bbac475. https://doi.org/10.1093/bib/bbac475
5. Stuart T, Srivastava A, Madad S. *et al.* Single-cell chromatin state analysis with signac. *Nat Methods* 2021;**18**:1333–41. https://doi.org/10.1038/s41592-021-01282-5
6. Zeng Y, Yin R, Luo M. *et al.* Identifying spatial domain by adapting transcriptomics with histology through contrastive learning. *Brief Bioinform* 2023;**24**:bbad048. https://doi.org/10.1093/bib/bbad048
7. Zhao E, Stone MR, Ren X. *et al.* Spatial transcriptomics at subspot resolution with Bayes space. *Nat Biotechnol* 2021;**39**:1375–84. https://doi.org/10.1038/s41587-021-00935-2
8. Zeng Y, Wei Z, Weijiang Y. *et al.* Spatial transcriptomics prediction from histology jointly through transformer and graph neural networks. *Brief Bioinform* 2022;**23**:bbac297. https://doi.org/10.1093/bib/bbac297
9. Dong K, Zhang S. Deciphering spatial domains from spatially resolved transcriptomics with an adaptive graph attention auto-encoder. *Nat Commun* 2022;**13**:1739. https://doi.org/10.1038/s41467-022-29439-6
10. Shan Y, Zhang Q, Guo W. *et al.* Tist: transcriptome and histopathological image integrative analysis for spatial transcriptomics. *Genom Proteom Bioinform* 2022;**20**:974–88. https://doi.org/10.1016/j.gpb.2022.11.012
11. Cutiongco MFA, Jensen BS, Reynolds PM. *et al.* Predicting gene expression using morphological cell responses to nanotopography. *Nat Commun* 2020;**11**:1384. https://doi.org/10.1038/s41467-020-15114-1
12. Dries R, Zhu Q, Dong R. *et al.* Giotto: a toolbox for integrative analysis and visualization of spatial expression data. *Genome Biol* 2021;**22**:1–31.
13. Shang L, Zhou X. Spatially aware dimension reduction for spatial transcriptomics. *Nat Commun* 2022;**13**:7203. https://doi.org/10.1038/s41467-022-34879-1
14. Xu H, Fu H, Long Y. *et al.* Unsupervised spatially embedded deep representation of spatial transcriptomics. *Genome Med* 2024;**16**:12. https://doi.org/10.1186/s13073-024-01283-x
15. Li J, Chen S, Pan X. *et al.* Cell clustering for spatial transcriptomics data with graph neural networks. *Nat Comput Sci* 2022;**2**:399–408. https://doi.org/10.1038/s43588-022-00266-5

16. Chang X, Jin X, Wei S. *et al.* Deepst: identifying spatial domains in spatial transcriptomics by deep learning. *Nucleic Acids Res* 2022;**50**:e131–1.
17. Xu H, Usuyama N, Bagga J. *et al.* A whole-slide foundation model for digital pathology from real-world data. *Nature* 2024;**630**:181–188. https://doi.org/10.1038/s41586-024-07441-w
18. Wang X, Zhao J, Marostica E. *et al.* A pathology foundation model for cancer diagnosis and prognosis prediction. *Nature* 2024;**634**:970–8. https://doi.org/10.1038/s41586-024-07894-z
19. Chung Y, Ha JH, Im KC, *et al.* Accurate spatial gene expression prediction by integrating multi-resolution features. In: *Proceedings of the IEEE/CVF Conference on Computer Vision and Pattern Recognition (CVPR)*. Piscataway, NJ: IEEE; 2024. p. 11591–11600.
20. Pham D, Tan X, Xu J. *et al.* stLearn: integrating spatial location, tissue morphology and gene expression to find cell types, cell-cell interactions and spatial trajectories within undissociated tissues. *bioRxiv* 2020:2020.05.31.125658. https://doi.org/10.1101/2020.05.31.125658
21. Jian H, Li X, Coleman K. *et al.* Spagcn: integrating gene expression, spatial location and histology to identify spatial domains and spatially variable genes by graph convolutional network. *Nat Methods* 2021;**18**:1342–51.
22. Zong Y, Yu T, Wang X. *et al.* conST: an interpretable multi-modal contrastive learning framework for spatial transcriptomics. *bioRxiv* 2022:2022.01.14.476408. https://doi.org/10.1101/2022.01.14.476408
23. Kim S, Bae S, Piao Y. *et al.* Graph convolutional network for drug response prediction using gene expression data. *Mathematics* 2021;**9**:772. https://doi.org/10.3390/math9070772
24. Lee S, Lim S, Lee T. *et al.* Cancer subtype classification and modeling by pathway attention and propagation. *Bioinformatics* 2020;**36**:3818–24. https://doi.org/10.1093/bioinformatics/btaa203
25. Xun Z, Ding X, Zhang Y. *et al.* Reconstruction of the tumor spatial microenvironment along the malignant-boundary-nonmalignant axis. *Nat Commun* 2023;**14**:933. https://doi.org/10.1038/s41467-023-36560-7
26. Andersson A, Larsson L, Stenbeck L. *et al.* Spatial deconvolution of HER2-positive breast cancer delineates tumor-associated cell type interactions. *Nat Commun* 2021;**12**:6012. https://doi.org/10.1038/s41467-021-26271-2
27. Rahman MN, Al Noman A, Turza AM. *et al.* Scribbledom: using scribble-annotated histology images to identify domains in spatial transcriptomics data. *Bioinformatics* 2023;**39**:btad594.
28. Oliveira MF, Romero JP, Chung M. *et al.* High-definition spatial transcriptomic profiling of immune cell populations in colorectal cancer. *Nat Genet* 2025;**57**:1512–1523. https://doi.org/10.1038/s41588-025-02193-3
29. Pardo B, Spangler A, Weber LM. *et al.* Spatiallibd: an r/bioconductor package to visualize spatially-resolved transcriptomics data. *BMC Genomics* 2022;**23**:434.
30. Kanehisa M, Goto S. Kegg: Kyoto encyclopedia of genes and genomes. *Nucleic Acids Res* 2000;**28**:27–30.
31. Zhang JD, Wiemann S. Kegg graph: a graph approach to KEGG pathway in r and bioconductor. *Bioinformatics* 2009;**25**:1470–1.
32. Paszke A, Gross S. *et al.* PyTorch: An imperative style, high-performance deep learning library. *Adv Neural Inf Process Syst* 2019;**32**:8026–8037.
33. Hamilton W, Ying Z, Leskovec J. Inductive representation learning on large graphs. *Adv Neural Inf Process Syst* 2017;**30**:1024–1034.
34. Huang G, Liu Z, Van Der Maaten L. *et al.* Densely connected convolutional networks. In: *Proceedings of the IEEE Conference on Computer Vision and Pattern Recognition (CVPR)*. Piscataway, NJ: IEEE; 2017. p. 4700–4708.
35. Deng J, Dong W, Socher R. *et al.* ImageNet: a large-scale hierarchical image database. In: *2009 IEEE Conference on Computer Vision and Pattern Recognition*, Piscataway, NJ: IEEE, pp. 248–255. 2009.
36. Chen T, Kornblith S, Norouzi M. *et al.* A simple framework for contrastive learning of visual representations. In: *International Conference on Machine Learning*, Vienna, Austria: PMLR, pp. 1597–1607. 2020.
37. Chuang C-Y, Robinson J, Lin Y-C. *et al.* Debiased contrastive learning. *Adv Neural Inform Process Syst* 2020;**33**:8765–75.
38. Rand WM. Objective criteria for the evaluation of clustering methods. *J Am Stat Assoc* 1971;**66**:846–50. https://doi.org/10.1080/01621459.1971.10482356
39. Strehl A, Ghosh J. Cluster ensembles—a knowledge reuse framework for combining multiple partitions. *J Mach Learn Res* 2002;**3**:583–617.
40. Moran PAP. Notes on continuous stochastic phenomena. *Biometrika* 1950;**37**:17–23. https://doi.org/10.1093/biomet/37.1-2.17
41. Alexander Wolf F, Hamey FK, Plass M. *et al.* PAGA: graph abstraction reconciles clustering with trajectory inference through a topology preserving map of single cells. *Genome Biol* 2019;**20**:1–9.
42. Hynes NE, Lane HA. ERBB receptors and cancer: the complexity of targeted inhibitors. *Nat Rev Cancer* 2005;**5**:341–54.
43. Badache A, Gonçalves A. The ErbB2 signaling network as a target for breast cancer therapy. *J Mammary Gland Biol Neoplasia* 2006;**11**:13–25. https://doi.org/10.1007/s10911-006-9009-1
44. Youle RJ, van der Bliek AM. Mitochondrial fission, fusion, and stress. *Science* 2012;**337**:1062–5. https://doi.org/10.1126/science.1219855
45. Lonard DM, O'Malley BW. Progesterone receptor signaling in breast cancer: a key node in the decision to proliferate or differentiate. *Endocr Rev* 2012;**33**:373–422.
46. Ashida H, Mimuro H, Sasakawa C. Shigella manipulates host immune responses by delivering effector proteins with type iii secretion system. *Front Immunol* 2015;**6**:219. https://doi.org/10.3389/fimmu.2015.00219
47. Elmore S. Apoptosis: a review of programmed cell death. *Toxicol Pathol* 2007;**35**:495–516.
48. Sudipto Mukherjee and colleagues. Immune rejection in cancer: rethinking the immunological constant of rejection. *Immunol Rev* 2017;**280**:117–28.
49. Lagier-Tourenne C, Cleveland DW. Rethinking ALS: the fus about tdp-43. *Cell* 2009;**136**:1001–4. https://doi.org/10.1016/j.cell.2009.03.006
50. Cleveland DW, Rothstein JD. From charcot to lou gehrig: deciphering selective motor neuron death in ALS. *Nat Rev Neurosci* 2001;**2**:806–19.
51. Drago JZ, Ferraro E, Abuhadra N. *et al.* Beyond her2: targeting the erbb receptor family in breast cancer. *Cancer Treat Rev* 2022;**109**:102436.
52. De Keulenaer GW, Doggen K, Lemmens K. The vulnerability of the heart as a pluricellular paracrine organ: lessons from unexpected triggers of heart failure in targeted erbb2 anticancer therapy. *Circ Res* 2010;**106**:35–46. https://doi.org/10.1161/CIRCRESAHA.109.205906
53. Roussos ET, Condeelis JS, Patsialou A. Chemotaxis in cancer. *Nat Rev Cancer* 2011;**11**:573–87. https://doi.org/10.1038/nrc3078
54. Vander MG, Heiden LC, Cantley, and Craig B Thompson. Understanding the Warburg effect: the metabolic requirements of cell proliferation. *Science* 2009;**324**:1029–33.

55. Pavlova NN, Thompson CB. The emerging hallmarks of cancer metabolism. *Cell Metab* 2016;**23**:27–47. https://doi.org/10.1016/j.cmet.2015.12.006
56. Dagogo-Jack I, Shaw AT. Tumour heterogeneity and resistance to cancer therapies. *Nature reviews. Clin Oncol* 2018;**15**:81–94. https://doi.org/10.1038/nrclinonc.2017.166
57. Hanahan D. Hallmarks of cancer: new dimensions. *Cancer Discov* 2022;**12**:31–46. https://doi.org/10.1158/2159-8290.CD-21-1059
58. Wang K, Li L, Liang F. *et al.* Integrated bioinformatics analysis the function of RNA binding proteins (RBPS) and their prognostic value in breast cancer. *Front Pharmacol* 2019;**10**:140. https://doi.org/10.3389/fphar.2019.00140
59. Marusyk A, Almendro V, Polyak K. Intra-tumour heterogeneity: a looking glass for cancer? *Nat Rev Cancer* 2012;**12**:323–34. https://doi.org/10.1038/nrc3261
60. Bedard PL, Hansen AR, Ratain MJ. *et al.* Tumour heterogeneity in the clinic. *Nature* 2013;**501**:355–64. https://doi.org/10.1038/nature12627
61. Kleshchevnikov V, Shmatko A, Dann E. *et al.* Cell2location maps fine-grained cell types in spatial transcriptomics. *Nat Biotechnol* 2022;**40**:661–71. https://doi.org/10.1038/s41587-021-01139-4
62. Regev A, Teichmann SA, Lander ES. *et al.* The human cell atlas.The human cell atlas. *elife* 2017;**6**:e27041. https://doi.org/10.7554/eLife.27041
63. Dongen S. A cluster algorithm for graphs. Netherlands: CWI (Centre for Mathematics and Computer Science), 2000.
64. Da Silva PL, Do Amaral VC, Gabrielli V. *et al.* Prolactin promotes breast cancer cell migration through actin cytoskeleton remodeling. *Front Endocrinol* 2015;**6**:186. https://doi.org/10.3389/fendo.2015.00186
65. Fiorillo AA, Medler TR, Feeney YB. *et al.* The prolactin receptor transactivation domain is associated with steroid hormone receptor expression and malignant progression of breast cancer. *Am J Pathol* 2013;**182**:217–33. https://doi.org/10.1016/j.ajpath.2012.09.021
66. Arellano A R-d, Villegas-Pineda JC, Hernández-Silva CD. *et al.* The relevant participation of prolactin in the genesis and progression of gynecological cancers. *Front Endocrinol* 2021;**12**:747810. https://doi.org/10.3389/fendo.2021.747810
67. Shah S, Brock EJ, Jackson RM. *et al.* Downregulation of rap1gap: a switch from dcis to invasive breast carcinoma via erk/mapk activation. *Neoplasia* 2018;**20**:951–63.
68. Zheng H, Gao L, Feng Y. *et al.* Down-regulation of rap1gap via promoter hypermethylation promotes melanoma cell proliferation, survival, and migration. *Cancer Res* 2009;**69**:449–57. https://doi.org/10.1158/0008-5472.CAN-08-2399
69. Fa-Xing Y, Zhao B, Guan K-L. Hippo pathway in organ size control, tissue homeostasis, and cancer. *Cell* 2015;**163**:811–28. https://doi.org/10.1016/j.cell.2015.10.044
70. Moroishi T, Hansen CG, Guan K-L. The emerging roles of yap and taz in cancer. *Nat Rev Cancer* 2015;**15**:73–9. https://doi.org/10.1038/nrc3876
71. Lee IY, Lim JM, Cho H. *et al.* Mst1 negatively regulates tnfα-induced nf-κb signaling through modulating lubac activity. *Mol Cell* 2019;**73**:1138–1149.e6. https://doi.org/10.1016/j.molcel.2019.01.022
72. Bos JL. Linking rap to cell adhesion. *Curr Opin Cell Biol* 2005;**17**:123–8. https://doi.org/10.1016/j.ceb.2005.02.009
73. Friedl P, Locker J, Sahai E. *et al.* Classifying collective cancer cell invasion. *Nat Cell Biol* 2012;**14**:777–83. https://doi.org/10.1038/ncb2548
74. Byrne KM, Monsefi N, Dawson JC. *et al.* Bistability in the rac1, pak, and rhoa signaling network drives actin cytoskeleton dynamics and cell motility switches. *Cell Syst* 2016;**2**:38–48. https://doi.org/10.1016/j.cels.2016.01.003
75. Sanz-Moreno V, Gadea G, Ahn J. *et al.* Rac activation and inactivation control plasticity of tumor cell movement. *Cell* 2008;**135**:510–23. https://doi.org/10.1016/j.cell.2008.09.043
76. Zhao J, Min W. Spaicl: image-guided curriculum strategy-based graph contrastive learning for spatial transcriptomics clustering. *Brief Bioinform* 2025;**26**:bbaf433.
77. Tang Z, Li Z, Hou T. *et al.* Sigra: single-cell spatial elucidation through an image-augmented graph transformer. *Nat Commun* 2023;**14**:5618. https://doi.org/10.1038/s41467-023-41437-w
78. Li B, Tang Z, Budhkar A. *et al.* SpaIM: Single-cell spatial transcriptomics imputation via style transfer. *bioRxiv* 2025:2025.01.24.634756. https://doi.org/10.1101/2025.01.24.634756

Briefings in Bioinformatics, 2026, **27**, bbag029
https://doi.org/10.1093/bib/bbag029
Problem Solving Protocol